Journal of Energy Storage 154 (2026) 121121

Contents lists available at ScienceDirect

Journal of Energy Storage

journal homepage: www.elsevier.com/locate/est

Research papers

Irida-Silicene as promising electrode material for supercapacitors. A comparative study by means of molecular dynamics

Hugo X. Rodrigues [a,b], Isabel A. Silva [c], Luiz A. Ribeiro Jr. [a,b,d], Marcelo L. Pereira Jr. [a,e], Leonardo J.A. Siqueira [c,d,*]

[a] University of Brasília, Institute of Physics, Physics Postgraduate Program, 70910900, Brasília, Federal District, Brazil
[b] Computational Materials Laboratory, University of Brasília, 70910900, Brasília, Federal District, Brazil
[c] Hybrid Materials Laboratory, Chemistry Department, Institute of Environmental Science, Chemical, and Pharmaceutical, Federal University of São Paulo, 09913-030, Diadema, São Paulo, Brazil
[d] University of Brasília, Institute of Physics, 70910900, Brasília, Federal District, Brazil
[e] University of Brasília, College of Technology, Department of Electrical Engineering, 70910900, Brasília, Federal District, Brazil

ARTICLE INFO

Keywords:
Two-dimensional allotropes
Irida-graphene
Irida-silicene
Supercapacitors
Classical molecular dynamics

ABSTRACT

Two-dimensional (2D) materials based on carbon and silicon have received considerable attention as potential electrode candidates for supercapacitors due to their structural and electrochemical properties. In this study, fully atomistic molecular dynamics simulations were performed for four symmetric supercapacitors constructed with Graphene, Irida-Graphene, Silicene, and Irida-Silicene as electrodes. The constant potential model was employed to simulate the electrode polarization under an applied voltage. The silicon-based supercapacitors showed improved performance in terms of power density and energy density when compared with the carbon-based systems. The specific capacitance (F/g) obtained for the former is approximately 50 % higher than that of the latter, even though Si atoms are twice as heavy as C atoms. This result is related to the intrinsic roughness of the silicon-based 2D materials, which enhances charge polarization at the electrodes. As a consequence, in addition to the increase in capacitance, a reduction in cell resistance is also observed due to the stronger interaction between the electrolyte counter-ions and the electrode surface. The work further presents a detailed analysis of the electrolyte structuring, providing insights into why silicon-based materials can be considered suitable alternatives for the development of high-performance supercapacitors.

1. Introduction

Two-dimensional (2D) materials have attracted substantial attention over the past two decades owing to their physical, chemical, and electronic properties, enabling a wide range of applications in nanoelectronics, optoelectronics, sensing, catalysis, and energy storage and conversion [1–4]. Their reduced dimensionality, high specific surface area, and tunable band structures allow the design of devices with superior performance compared to their three-dimensional (3D) counterparts [5,6].

Within this class, carbon-based 2D materials occupy a central role, with graphene being the most prominent example due to its electrical, thermal, and mechanical properties [7–9]. Beyond graphene, several carbon allotropes have been theoretically predicted and subsequently synthesized [10–14], many of which exhibit promising features for next-generation technologies. In parallel, silicon-based 2D materials, such as silicene, have emerged as attractive alternatives, offering compatibility with existing silicon-based microelectronics while displaying electronic properties distinct from those of their carbon analogues [15–17].

Among the carbon allotropes proposed in recent years, Irida-Graphene (Irida-Gr) stands out as a 2D material composed of a 3-6-8 ring network [18], which has recently become the focus of several studies. In addition to previously reported structural, electronic, optical, and mechanical characterizations [18], reactive molecular dynamics simulations have shown that Irida-Gr exhibits an intrinsic thermal conductivity at room temperature of approximately 215 W m^{-1} K^{-1}, with transport regimes ranging from ballistic to diffusive [19]. On the other hand, Li and co-workers also used molecular dynamics simulations to investigate the mechanical response of monolayer and multilayer Irida-Gr under tensile loading, including the effects of pre-existing cracks [20].

* Corresponding author at: Hybrid Materials Laboratory, Chemistry Department, Institute of Environmental Science, Chemical, and Pharmaceutical, Federal University of São Paulo, 09913-030, Diadema, São Paulo, Brazil.
E-mail addresses: ribeirojr@unb.br (L.A. Ribeiro Jr.), ljasiqueira@unifesp.br (L.J.A. Siqueira).

https://doi.org/10.1016/j.est.2026.121121
Received 11 September 2025; Received in revised form 16 January 2026; Accepted 15 February 2026
Available online 20 February 2026

Beyond its physicochemical characterization, the porous nature of Irida-Gr favors atomic and molecular adsorption and storage processes for diverse applications. In this regard, density functional theory (DFT) calculations have indicated that decoration with transition metals such as Sc, Ti, V, and Nb enables reversible H_2 adsorption with suitable binding energies [21,22]. Laranjeira et al. [23] demonstrated that functionalization with the superalkali OLi_3 allows hydrogen storage capacities of up to 10.0 wt% under ambient conditions. Other works have reported that Irida-Gr exhibits high storage capacity when decorated with alkali metals, as well as with Li [24,25], Na [24,26,27], Ca [28], and K [24], achieving high reversible capacities.

In the field of electrochemical energy storage, Irida-Gr has also shown significant potential as an electrode material. Xiong and coworkers predicted that monolayer Irida-Gr can function as an efficient anode for lithium-ion batteries (LIBs) [29], offering high stability, excellent conductivity, and low diffusion barriers for Li^+. Comparable performance has been reported for sodium-ion batteries (SIBs) by Kaur et al. [30] and Martins et al. [31]. While Wei and colleagues investigated the material for multi-alkali systems (Li/Na/K) [32], confirming high theoretical capacities and rapid ion transport. Rusho and collaborators extended these investigations to magnesium-ion batteries (MIBs) [33] and potassium-ion batteries (PIBs) [34], the latter studied in a boron nitride analogue of Irida-Gr. For Li–S batteries, Martins et al. [35] demonstrated that Irida-Gr strongly adsorbs polysulfides, mitigating the shuttle effect and further evidencing the versatility of this material in energy-related applications.

Structural variations of Irida-Gr have also been proposed, including Irida-Graphyne [36], Twin-Irida [37], boron-nitride Irida (Irida-BN) [38], and Irida-Silicene (Irida-Si) [39], the latter being a silicon-based analogue with larger pores and higher surface roughness, characteristics that may enhance adsorption processes.

Although the literature on Irida-Gr has grown rapidly, previous computational investigations have predominantly focused on battery-related applications or static adsorption phenomena, neglecting the dynamic response of electrified interfaces. Consequently, its potential as an electrode material for supercapacitors remains unexplored, with no systematic link established between atomistic dynamics and macroscopic performance metrics. This gap is even more pronounced for Irida-Si, which, despite its larger pores and higher intrinsic surface roughness, features that could enhance ion adsorption and charge storage, has not been considered in this context. Unlike earlier MD studies that predominantly address hexagonal graphene [40] or silicene [41], this study presents a direct and systematic comparison of hexagonal and Irida-like 2D architectures for carbon- and silicon-based electrodes. By evaluating all four structures, graphene, Irida-graphene, silicene, and Irida-silicene, under identical simulation protocols and using a single electrolyte and constant-potential methodology, we clarify the distinct influences of chemical composition and atomic-scale geometry on capacitive properties. This methodology uncovers a morphology-dependent mechanism absent from earlier MD reports: the non-hexagonal ring arrangement and inherent corrugation in Irida-type lattices intensify charge localization, bolster electrode–electrolyte coupling, and decrease interfacial resistance.

In this work, we systematically evaluating the capacitive performance of Irida-Gr and Irida-Si using a fully atomistic simulation framework. The methodology integrates classical molecular dynamics simulations with explicit electrode–electrolyte interfaces, where both materials are modeled as fully periodic porous electrodes in contact with an organic electrolyte. The simulations capture ion adsorption dynamics, charge accumulation processes, and potential-dependent behavior, enabling the direct estimation of key performance metrics such as differential capacitance, energy and power density, and ion transport characteristics. This approach provides a rigorous and quantitative comparison between Irida-Gr and Irida-Si, elucidating the influence of pore size and surface roughness on electrochemical performance and identifying their specific advantages relative to more established 2D materials such as graphene and silicene.

Table 1
Details of the simulation cells. Number of ion pairs, solvent molecules, and electrode atoms. L is the electrode separation in Å.

Electrode	# Ion pairs	# Solvent molecules	# Electrode atoms	L (Å)
Graphene	200	2000	512	276
Irida-Gr	200	2000	576	214
Silicene	200	2000	448	118
Irida-Si	200	2000	432	112

2. Methodology

This study investigates supercapacitors with 2D electrodes in honeycomb and Irida networks of carbon and silicon by means of fully atomistic molecular dynamics simulations. The electrolyte adopted was $1\,\mathrm{mol\,L^{-1}}$ $NaPF_6$ in a (1:1) mixture of ethylene carbonate (EC) and diethyl carbonate (DEC) [42], a standard formulation for high-voltage sodium- and lithium-ion devices [43]. This electrolyte provides a broad electrochemical stability window up to 3 V, enabling realistic evaluation of the modeled supercapacitors' energy and power densities [44]. It is worth noting that aqueous electrolytes are limited to approximately 1 V [45]. Furthermore, reliable non-polarizable force-field parameters are available in the literature for Na^+, $PF_6{}^-$, EC, and DEC [46–48], ensuring accurate description of ion–solvent and ion–electrode interactions. The electrolyte was confined between two conducting sheets, which enabled the observation of the electrode/electrolyte interface and the formation of the electrical double layer, supporting the estimation of capacitance, power, and stored energy.

The overall configuration is illustrated in Fig. 1. The top panel shows a snapshot of a polarized symmetric supercapacitor with electrode atoms colored by partial charge. The gray, semitransparent surface is a solvent-density isosurface constructed from the EC and DEC atomic positions, delineating the liquid region. The Na^+ and $PF_6{}^-$ species are shown explicitly as spheres immersed in this phase. The inserts on the right report the lateral dimensions of the electrode sheets and highlight the buckled character of the silicon-based materials, which is not observed for the carbon-based sheets. The bottom schematic depicts the periodic cell with 100 Å vacuum regions placed beyond the electrodes along z to suppress interactions between periodic images.

Initial geometries were generated with PACKMOL [49] and prepared with FFTOOL [50]. The lateral dimensions of each electrode were defined based on the rectangular unit cell of the corresponding material, which produced supercells with comparable extents in both the x and y directions. The separation between the conducting sheets, denoted L, ranged from 112 to 276 Å to reproduce within the cell the density of the neat electrolyte at 350 K. Two 100 Å vacuum regions were placed beyond the electrodes along z to remove coupling between periodic images. Table 1 lists the numbers of ion pairs, solvent molecules, and electrode atoms together with the values of L.

The choice of salt followed previous results indicating favorable performance of electrolytes with small ions in electrochemical energy-storage devices [51–55]. Lithium bis(trifluoromethanesulfonyl)imide in propylene carbonate delivers higher stored energy than conventional electrolytes, such as $TEABF_4$ [56]. Its high cost motivates the evaluation of more accessible alternatives. Sodium is more abundant in the Earth's crust, and $NaPF_6$ has been widely examined in sodium-ion batteries, which supports its use in supercapacitors as well.

Interaction parameters for the ions were taken from the CL&P force field for ionic liquids [46] and atomic charges were rescaled to $0.8\,e$. This strategy accounts for the electronic polarizability of the ions, especially for anions [47], and improves agreement with experiments for dynamical properties such as viscosity and ionic conductivity [42,57]. Parameters for the organic solvents were adapted from the AMBER, parm94, and OPLS force fields following the initial parameters of Takeuchi et al. for propylene carbonate [48]. Interactions with the electrode sheets were modeled with Lennard-Jones (LJ) parameters of

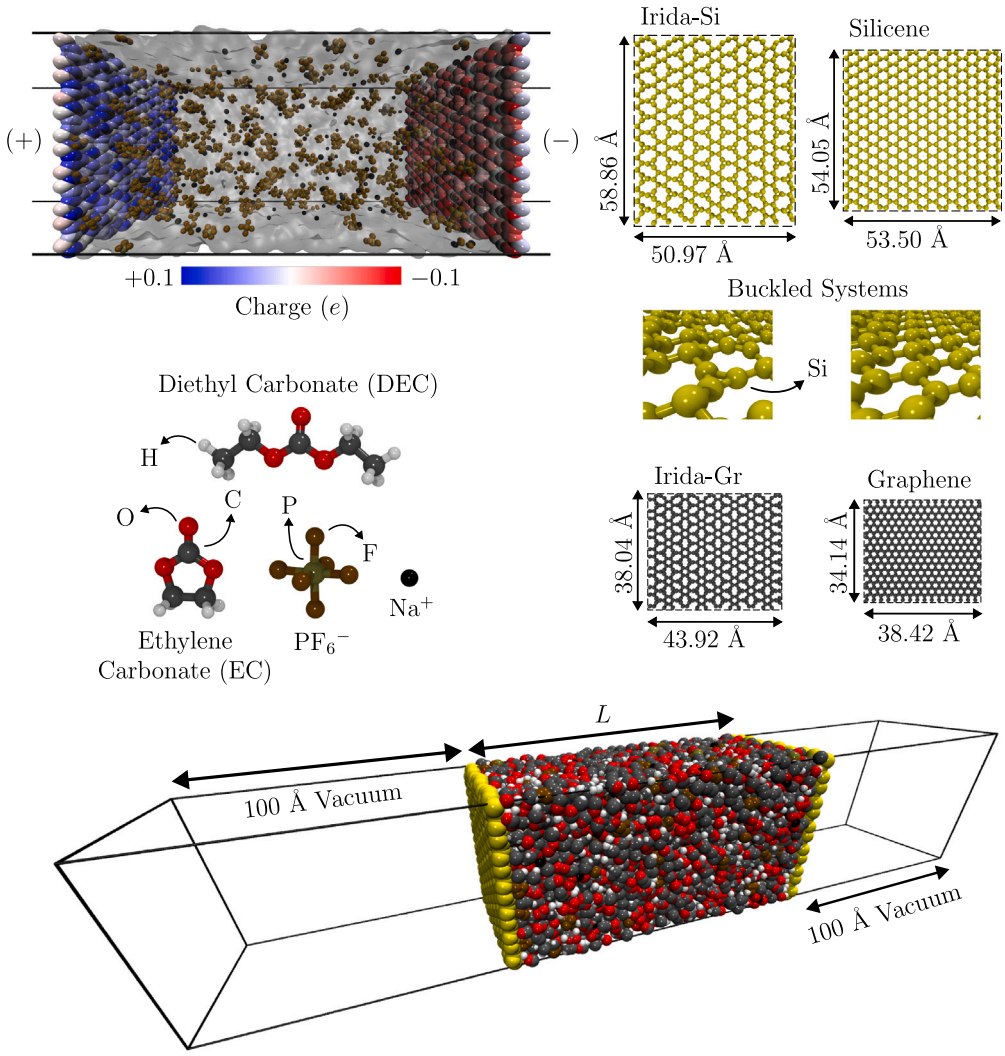

Fig. 1. Overview of the modeled system. Snapshot of a polarized symmetric supercapacitor with electrode atoms colored by partial charge. The gray, semitransparent surface is the solvent-density isosurface obtained from EC and DEC positions, marking the liquid region. Na^+ and PF_6^- are shown explicitly as spheres immersed in this phase. Inserts report the lateral dimensions of the electrode sheets and a detail of the buckled morphology in silicon-based materials. The periodic cell includes 100 Å vacuum regions beyond the electrodes along z. (For interpretation of the references to color in this figure legend, the reader is referred to the web version of this article.)

$\epsilon = 0.0699\,\text{kcal mol}^{-1}$ and $\sigma = 3.5500$ Å for carbon [58] and $\epsilon = 0.4023\,\text{kcal mol}^{-1}$ and $\sigma = 3.8264$ Å for silicon [59]. The Gaussian charge parameter was $1.015\,\text{Å}^{-1}$. Long-range electrostatics were treated using the particle–particle-particle-mesh (PPPM) method [60,61] in conjunction with the Yeh–Berkowitz slab correction [62] for 2D periodic boundary conditions.

Simulations were carried out in the canonical ensemble at 350 K with a time step of 2 fs and a Nosé–Hoover thermostat with a coupling time of 100 fs [63,64]. A cutoff of 12.0 Å was applied to Lennard-Jones interactions and to the real-space part of electrostatics. Bonds involving hydrogen were constrained with the SHAKE algorithm [65]. Each system was equilibrated for 10 ns at zero constant charge and then subjected to applied voltages using the constant potential method implemented in the ELECTRODE module of LAMMPS [66–68]. The charges of the atoms belonging to the electrodes were allowed to fluctuate for at least 4 ns, this time was sufficient to achieve complete charging, as shown in the next section, since a previous simulation of 10 ns guaranteed full equilibration of the electrolyte at zero charge, as cited above. For each voltage, two independent replicas were generated with different seeds. Structural analyses used the last half of the trajectories, and final values were obtained as averages over the replicas.

3. Results and discussions

3.1. Electrical properties

The electrode materials used in this study exhibit metallic properties, as evidenced by the absence of a band gap in the density of states calculated via DFT [15,69,70]. Therefore, the constant potential model can be employed to study the performance of supercapacitors containing these materials as electrodes. Fig. 2 shows the specific charge (C/g) accumulated on the electrodes (sum of each charge on the electrode atoms normalized by the electrode mass) at several applied voltages for the different supercapacitors. The higher the applied voltage, the higher the charge stored on the electrodes. After approximately 2 ns, a plateau appears in the charge curves, indicating that the supercapacitors are fully charged after this simulation time. The Irida-Gr and Irida-Si devices exhibit higher charge storage capacities than Graphene and Silicene, respectively, owing to their lower areal density. Among all the devices, the Irida-Si supercapacitor presents a superior charge storage performance, which can be attributed to its buckling, as this structural feature introduces surface roughness and enables greater ionic charge storage. The effect of buckling can be better understood

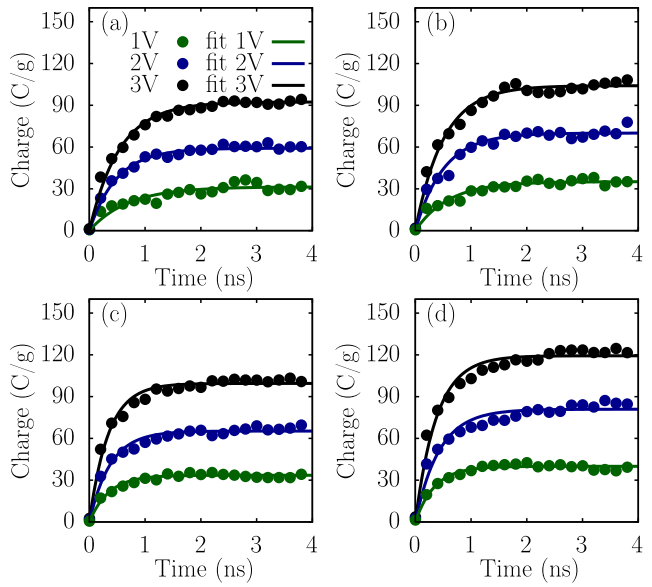

Fig. 2. Accumulated specific charge curves (dots) on the electrodes at different applied potentials for (a) Graphene, (b) Irida-Gr, (c) Silicene, and (d) Irida-Si devices. The lines are best-fit curves of a monoexponential function, Eq. (1).

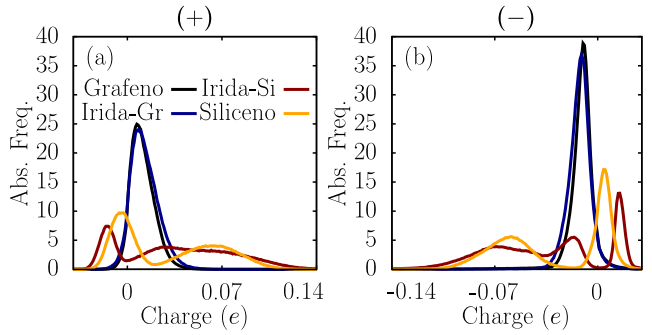

Fig. 3. Normalized absolute frequency of charge in (a) the positive and (b) the negative electrode for each supercapacitor at 3 V.

by the charge distribution on the electrodes upon the application of voltage, Fig. 3. Atoms in silicon-based electrodes can be more polarized and show higher partial charges than those in carbon-based ones. These findings support the idea that electrodes with rough surfaces can yield devices with enhanced charge storage capacity, consistent with previous molecular simulations of supercapacitors addressing this phenomenon [71–73].

Molecular dynamics simulations of supercapacitors aimed at studying charging dynamics often employ an equivalent circuit based on the transmission line model (TLM) to fit the charge stored in porous electrode [42,54,55,74–77]. In many of these studies, the electrodes are divided into two slices, leading to a biexponential function as the solution to the differential equation for two RC circuits connected in series [74,75]. In this study, however, we employed a monoexponential function (Eq. (1)), which corresponds to the solution of a simpler model involving a single RC circuit. This choice was motivated by our goal of comparing different devices with electrodes that are less complex than porous ones. Table 2 shows the best-fit parameters obtained for the monoexponential function, Eq. (1), the charge accumulated on the electrodes along the simulation time,

$$Q(t) = Q_{max}\left[1 - \exp\left(-\frac{t}{\tau}\right)\right], \tag{1}$$

where Q_{max} is the charge in the limit of $t \to \infty$, and τ is the relaxation charging time. For the carbon-based supercapacitors (Graphene and Irida-Gr), the relaxation times do not follow a monotonic trend, as $\tau(2V) < \tau(3V) < \tau(1V)$. In the case of Silicon-based ones, there is no clear trend, but $\tau(2V)$ values are larger than those obtained at $\Delta\Psi$ equals to 1 and 3 V. Previous molecular dynamics simulations of supercapacitors based on ionic liquids with graphite electrodes [42] and fullerene-decorated graphene electrodes [53] also consider that τ does not follow a monotonic relationship with the applied voltage, which is related to the charging mechanism changing with voltage.

Table 2
Charge accumulated on the electrodes normalized by their weight (in $C\,g^{-1}$) and charging time (τ in ps) calculated for different supercapacitors at several applied voltages.

Supercapacitor	1V		2V		3V	
	Q_{max}	τ	Q_{max}	τ	Q_{max}	τ
Graphene	31.42	695.82	59.17	489.71	92.38	540.97
Irida-Gr	35.17	595.87	70.06	501.76	104.12	505.05
Silicene	33.52	348.44	64.26	374.53	99.46	339.61
Irida-Si	39.94	344.27	80.95	427.52	119.36	382.60

Table 3
Differential capacitance on the positive and negative electrodes in $\mu F/cm^2$ calculated for different supercapacitors.

System	C^+	C^-
Graphene	4.930	3.601
Irida-Gr	5.312	3.775
Silicene	4.492	3.857
Irida-Si	5.475	4.591

The differential capacitance on the negative and positive electrodes is calculated by

$$C_d^{\pm} = \frac{d\sigma_{ele}^{\pm}}{d\Psi^{\pm}}, \tag{2}$$

where $\sigma^{\pm}$ is the real mean surface charge on the electrode,

$$\Delta\Psi = \Psi^{\pm} - \Psi^{bulk} - PZC, \tag{3}$$

is the potential at the electrode–electrolyte interface, and the PZC corresponds to the potential of zero charge, that is, the potential at which the surface carries no net charge. Table 3 presents the differential capacitances obtained from the slopes of the linear fits to the electrode charge density as a function of the potential drop across the cell. The differential capacitance of the positive electrodes is consistently higher than that of the negative electrodes, reflecting the larger potential drop on the negative side, as illustrated in Fig. 4. Fig. S1, S2, and S3 of the Supplementary Materials also show the potential drop across the cells containing Graphene, Irida-Gr, and Silicene electrodes. The potential drop was calculated by integrating the Poisson equation, as we have done in previous studies of our group [51,53,55,73]. Irida-based supercapacitors outperform those based on Graphene and Silicene, which is a manifestation of their higher charge storage capacity shown in Table 2. In particular, Irida-Si supercapacitors exhibit the best overall performance among all systems studied. Furthermore, the differential capacitances calculated here are consistent with those calculated for ionic liquids confined to graphite [42,78–80], graphene oxide [73,81], and planar MXenes electrodes [54].

Effective ion accumulation (EIA) is an interesting way of investigating the overscreening of the electrodes proposed in the simulations of ionic liquids as electrolytes for supercapacitors. The EIA of ionic liquids is characterized by strong oscillations that fade away towards the bulk region of the electrolyte [42,80,82]. Such oscillatory behavior of EIA comes from the alternating layer of ions close to the electrode surface upon the application of voltage. The charge of the first layer of counter-ion (ions with opposite charge to the electrode) adsorbed on the electrode is larger than that needed to screen the electrode charge, giving rise to the so-called charge overscreening. Thus, a second layer of co-ions (ions with the same charge as the electrode) is

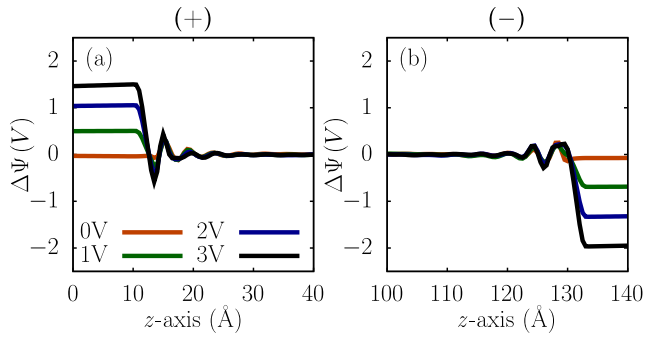

Fig. 4. Electrostatic potential profiles, $\phi(z)$, calculated for the Irida-Si supercapacitor as a function of the distance, z, at different applied voltages, near (a) the positive and (b) the negative electrode.

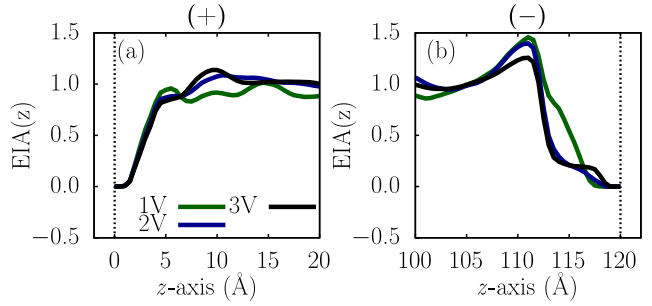

Fig. 5. Effective ion accumulation (EIA) calculated for Irida-Si at different applied voltages near (a) the positive and (b) the negative electrode.

formed to compensate for the charge excess of the adlayer. In its turn, the second layer of co-ion still has an excess charge. Therefore, a third layer of counterions is formed, and so on, until the electrolyte thoroughly screens the electrode charge. Beyond that, Merlet and co-workers [83] have proposed that porous electrodes outperform planar ones in terms of charge storage due to the confinement inside the pores, which prevents the occurrence of overscreening effects. Therefore, we calculate the effective ion accumulation for the supercapacitors investigated here. Fig. 5 shows the EIA across the cell containing Irida-Si as the electrode, indicating larger overscreening close to the negative electrode (EIA > 1), and, consequently, smaller capacitance in this electrode, as discussed before. Additionally, the EIA calculated here, using 1.0 mol L^{-1} $NaPF_6$ in EC:DEC shows that the electrode charge is thoroughly screened up to 10 Å from the electrode (EIA ≈ 0), that is, in shorter distance than in ionic liquids as electrolytes, in which the EIA tends to zero only after 30 Å far from the electrode. Figures S4 to S6 of the supplementary material show the EIA calculated for Graphene, Irida-Gr, and Silicene supercapacitors.

The resistance R is an important property to evaluate the performance of supercapacitors concerning the rate of energy delivery (power). Considering that we used a model containing only one RC circuit, the resistance, R, can be estimated by:

$$\tau = RC, \tag{4}$$

where τ is the relaxation charging time obtained from the fitting of the monoexponential function, and C is the capacitance, which is calculated from [84]

$$C = \frac{2Q_{max}}{\Delta\Psi \cdot m}, \tag{5}$$

where Q_{max} is the charge obtained from the fitting of charge curves, $\Delta\Psi$ is the applied potential, and m is the mass of both electrodes. Table 4 presents the cell resistances and specific capacitances calculated for the supercapacitors investigated here as a function of the applied voltage. At all applied voltages, the specific capacitances of irida-based supercapacitors are higher than those calculated for silicene and graphene.

Table 4
Capacitances (C in F g^{-1}) and resistances (R in 10^8 Ω) calculated for the supercapacitors at several applied voltages.

Supercapacitor	1V		2V		3V	
	R	*C*	*R*	*C*	*R*	*C*
Graphene	21.7	31.42	16.2	29.59	17.2	30.59
Irida-Gr	14.8	35.17	12.5	35.03	12.7	34.70
Silicene	4.99	33.52	5.59	32.15	4.92	33.15
Irida-Si	4.29	39.94	5.26	40.47	4.79	39.78

Among the devices investigated, the Irida-Si supercapacitor exhibits the highest capacitance. Although silicene is heavier, it outperforms graphene in terms of capacitance, albeit with slightly higher resistance.

The differential capacitance obtained for the graphene electrode (≈4.9 μF cm^{-2}) is in good agreement with molecular dynamics [85] and DFT [86,87] simulations, as well as with experimental results [88] for graphene/ionic-liquid interfaces (typically in the range of 4–10 μF cm^{-2}). Moreover, the specific capacitance values calculated in this study is close to previous molecular dynamics simulations of supercapacitors with ionic liquids confined in graphite (30 F g^{-1}) [83]. Also, the specific capacitance of graphene (≈31 F g^{-1} at 1 V) falls within the experimentally reported range of thermally reduced graphene-sheets supercapacitors employing organic electrolytes (25–50 F g^{-1}) [89]. This agreement validates the simulation model and supports the subsequent analysis of Irida-type electrodes.

The enhanced capacitance observed for silicene and Irida-silicene arises from their intrinsic out-of-plane buckling, which effectively represents surface roughness in our defect-free, frozen-lattice simulations. Silicene and Irida-silicene exhibit buckling amplitudes of 0.44 Å and 0.78 Å [69,90], respectively, whereas graphene and Irida-graphene remain atomically flat and therefore display zero surface roughness. Furthermore, the quantum capacitances of silicon-based and carbon-based materials are, respectively, 364 and 355 F g^{-1} at 3 V, as supported by previous studies [72,91]. These values yield a negligible contribution to the total capacitance of the devices. Therefore, quantum capacitances were not considered in the present study.

This built-in corrugation enhances local polarization and promotes more pronounced ion layering at the interface, in agreement with the charge and density profiles obtained from constant-potential simulations.

The performance of electrochemical cells in terms of energy and power densities is often evaluated together by the Ragone plot, which is calculated by using [92]

$$E(P) = \frac{1}{2}C\left[RP\ln\left(\frac{RP}{U^2}\right) + U^2 - RP\right], \tag{6}$$

where $E(P)$ is the energy density, P is the power density, R is the cell resistance, C is the capacitance and U is the constant voltage of the reversible cell given by [92]:

$$U = \frac{U_c}{2} + \sqrt{\frac{U_c^2}{4} - RP}, \tag{7}$$

where U_c is the applied voltage.

The cell resistance can be calculated using Eq. (4), where τ_{macro} is the charging time for an electrode at the macroscopic scale, estimated by $\tau_{macro} = \tau[(l_{macro}/l)]^2$, where l and l_{macro} represent the electrode size in the system used in the simulation and its macroscopic size, respectively. Here we have used l =10 Å for all the supercapacitors to make a fair comparison, considering that carbon-based electrodes are flat, whereas the silicon-based ones present buckling. This scaling assumes that the charging mechanism remains diffusion-limited and that the electrode morphology is uniform at larger scales. It should be noted that our model does not account for macroscopic resistive losses (e.g., contact resistance, binder effects, or electrolyte resistance outside the pores), which would reduce power density in practical devices.

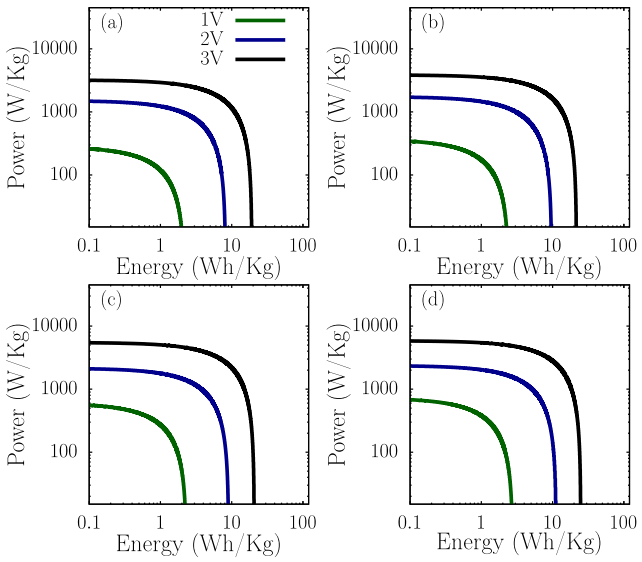

Fig. 6. Comparison between power and energy densities (Ragone plot) for (a) Graphene, (b) Irida-Gr, (c) Silicene, and (d) Irida-Si supercapacitors at different applied voltages.

Nevertheless, the relative trends among the four materials are robust and provide valuable guidance for material selection.

The Ragone plots in Fig. 6 show energy and power densities normalized by the total mass of the symmetric electrodes, as calculated using Eqs. (5) and (6). Energy and power densities increase with the applied voltage. At high voltage, the energy stored in the supercapacitors is around 38.4 and 49.7 $W\,h\,kg^{-1}$, while power spans from 6410 to 11 700 $W\,kg^{-1}$. The maximum energy and power densities calculated for the supercapacitors are presented in Table S1 of the supplementary materials. Graphene cells present the worst performance, whereas Irida-Si supercapacitors present the best performance in terms of energy and power. The range of energy and power densities calculated for the supercapacitors investigated here is comparable with the performance of supercapacitors containing ionic liquids confined in electrodes of graphene decorated with fullerene [53].

These findings fall close the range reported for state-of-the-art experimental carbon-based materials, where devices based on graphene, porous carbon nanosheets, or heteroatom-engineered carbons typically exhibit energy densities between 5 and 20 $W\,h\,kg^{-1}$ and power densities ranging from 1 to 10 $kW\,kg^{-1}$ [40,45,93]. They are also comparable to Ragone plots obtained from electrochemical experiments employing 1.0 $mol\,L^{-1}$ tetraethylammonium tetrafluoroboride in propylene carbonate confined in activated carbon, which reported maximum power and energy densities of 2570 $W\,kg^{-1}$ and 7.52 $W\,h\,kg^{-1}$, respectively [56]. Therefore, the modeled systems are consistent with the upper end of the experimental performance envelope, as expected for atomically flat, defect-free 2D electrodes operating across the full stability window of an organic electrolyte.

3.2. Structure and interaction energy at electrolyte–electrode interface

The way the electrolytes are structured in the vicinity of electrodes determines the supercapacitors' performance. Therefore, in order to figure out the best performance of Irida-Si among the others, we calculated number density profiles of ions and solvent molecules across the z-axis of the cell at $\Delta\Psi = 0$ and 3 V for this system, Fig. 7. At null charge ($\Delta\Psi = 0$ V), the surface of the electrodes is mainly covered by carbonate solvent molecules, with a small amount of $NaPF_6$. A second layer arises around 7 Å far from the electrodes that has a higher density of the salt. At the end of the charging procedure (after 2 ns), there is a

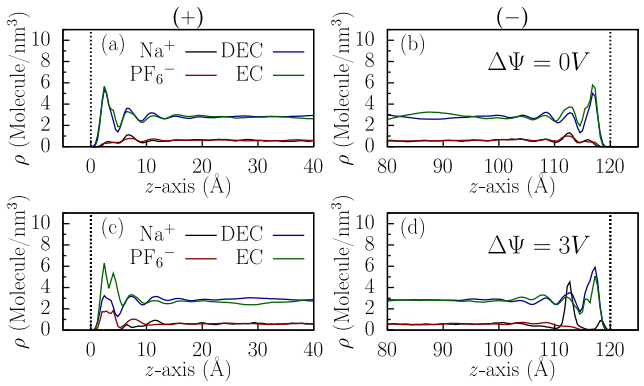

Fig. 7. Number density profiles of ions and solvent molecules (Na^+, PF_6^-, DEC, and EC) across the z-axis of the simulation box at $\Delta\Psi = 0$ and 3 V for Irida-Si device near (a,c) the positive and (b,d) the negative electrode. The dotted line indicates the position of the electrodes.

layer of PF_6^- with a thickness of ≈5 Å on the surface of the positive electrode to screen the charge. Only from ≈5 Å towards the bulk region of the electrolyte Na^+ can be found. Given the stronger interaction between Na^+ and DEC (See Figure S14 of the Supplementary Materials), the cations repelled from the positive electrode bring together DEC molecules of its coordination shell towards the bulk, explaining the richer layer of EC on the surface of the positive electrode. On the other side of the cell, the negative electrode, there is a layer with a thickness of ≈6 Å of Na^+, DEC, and EC. Note that the layer of solvent molecules adsorbed on the negative electrode is richer in DEC. A second and rich layer of Na^+ arises farther from the negatively charged surface (around z-axis ≈112 Å). Again, this feature is related to the strong Na-O_{DEC} interaction and the repulsion between the negative electrode and the oxygen atoms (negatively charged) of DEC, prompting a rearrangement of DEC molecules adsorbed on the electrode surface. The closest layer of anions near the negative surface of the electrode only appears after the first layer of Na^+ directly adsorbed onto the surface of the negative electrode due to the electrostatic repulsion. Similar features are observed in Figures S7-S9, which present the number density profiles calculated for graphene, silicene, and Irida-Gr at $\Delta\Psi = 3$ V.

Further investigation of the density profiles within the adlayer enables a detailed analysis of how its structure changes upon application of voltage. Therefore, we calculate the difference between the number of molecules within this layer at a given voltage and the number at 0 V (ΔN), where the layer thickness was chosen based on the high density of these adsorbed molecules. In both electrodes, there is ion exchange at the electrode–electrolyte interface; that is, the number of counter-ions (ions with opposite charge to the electrode) increases, while the number of co-ions (ions with the same charge as the electrode) decreases. In the positive electrode, the number of PF_6^- increases more than the number of co-ions decreases. It is interesting that in both electrodes, the number of EC increases, while the number of DEC decreases in the closest layer of electrolyte in direct contact with the electrodes. Similar behavior has been found in the other investigated supercapacitors as depicted in Figures S11 to S13 of the Supplementary Materials.

Fig. 9 shows the coordination number of Na^+ $n(r)$, calculated for fluorine and oxygen atoms from PF_6^-, DEC and EC within a radius of 3.5 Å around Na^+ in the bulk region and inside the 10-Å-layer near the negative electrode at $\Delta\Psi = 3$ V. Despite the enrichment of EC on the electrode surfaces upon the applied voltage, shown in Fig. 8, the local environment of Na^+ near the negative electrode surfaces resembles the one found in the bulk region of the simulation cell, where the effect of the applied voltage is negligible.

Fig. 10 shows the short-range interaction energies (Lennard-Jones and Coulomb terms) up to 12 Å as a function of the simulation times. Upon applying voltage, the interaction energies between electrodes

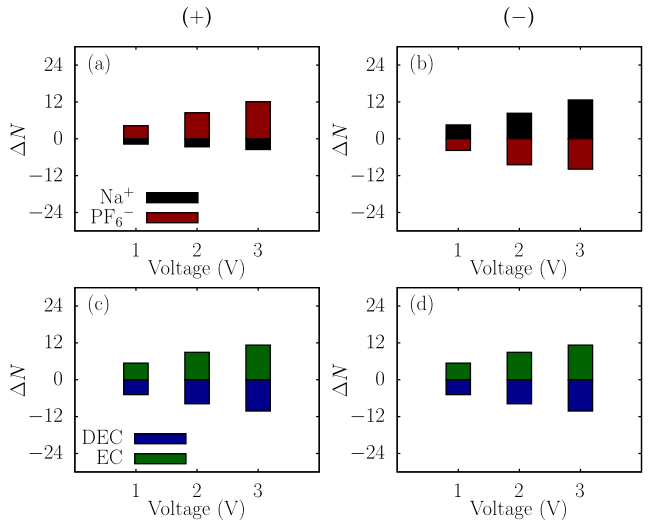

Fig. 8. Number of molecules adsorbing ($\Delta N > 0$) or desorbing ($\Delta N < 0$) on the surface of Irida-Si at different applied voltages. The layer thicknesses used to calculate these numbers for the different species are in parentheses. Positive electrode (a) and (c): Na^+ (5 Å), PF_6^- (5 Å), DEC (5 Å), EC (6 Å). Negative electrode (c) and (d): Na^+ (10 Å), PF_6^- (10 Å), DEC (6 Å), EC (6 Å).

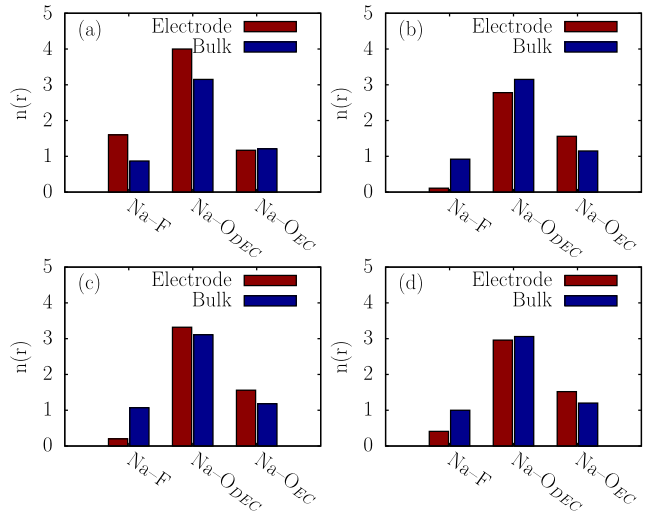

Fig. 9. Coordination numbers of Na^+, $n(r)$, calculated for fluorine and oxygen atoms from PF_6^-, DEC and EC within a radius of 3.5 Å around of Na^+ in the bulk region and inside the 10-Å-layer near the negative electrode, where the ions are subjected to a potential of $\Delta\Psi = 3$ V. Data are shown for (a) Graphene, (b) Irida-Graphene, (c) Silicene, and (d) Irida-Silicene.

and counter-ions become more substantial, particularly between the positive electrode and the anion. These interactions in Silicon-based supercapacitors (Fig. 10c and d) are even stronger than in carbon-based systems, which are related to stronger LJ interactions ($\epsilon_{Si} > \epsilon_C$) and the larger polarized charges on the Silicon-based electrodes, as illustrated in Fig. 3. The strong Na^+-solvent interaction shields the negative electrode and cation interactions, resulting in a minor contribution from these interactions compared to the electrode's positive and anion interactions. It is interesting to note that the repulsion between co-ions and electrodes is not as strong as the attraction between counter-ions and electrodes. Therefore, the ion exchange observed on the electrode's surface, as shown in Fig. 8a and b, can be determined by the attraction forces between the electrode and counter-ions.

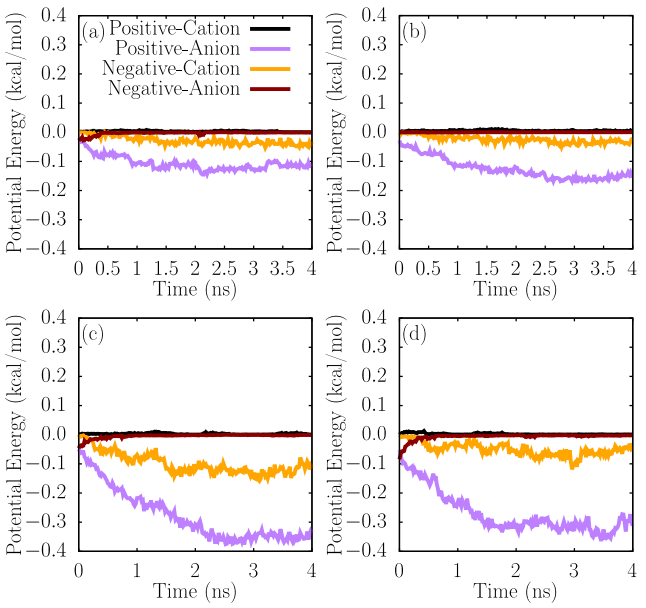

Fig. 10. Interaction energy (Lennard-Jones plus Coulomb) up to 12 Å between ions and electrode under voltage of $\Delta\Psi = 3$ V normalized by the number of electrode atoms along the charging simulation. Data for (a) Graphene, (b) Irida-Graphene, (c) Silicene, and (d) Irida-Silicene.

Considering that it was observed that there was a change in the number of solvent molecules at the electrode–electrolyte interface, Fig. 8c and d, we also calculated the solvent–electrode interactions for the supercapacitors investigated here. Fig. 11 shows that the interaction between the solvent molecules and the negative electrodes is barely affected upon the application of potential difference ($\Delta\Psi$). However, a weakening of the interaction between DEC and the positive electrode can be observed, which is particularly pronounced in silicon-based supercapacitors. Conversely, the interaction between EC and the positive electrode becomes stronger, which is consistent with the enrichment of EC on the surface of charged electrodes.

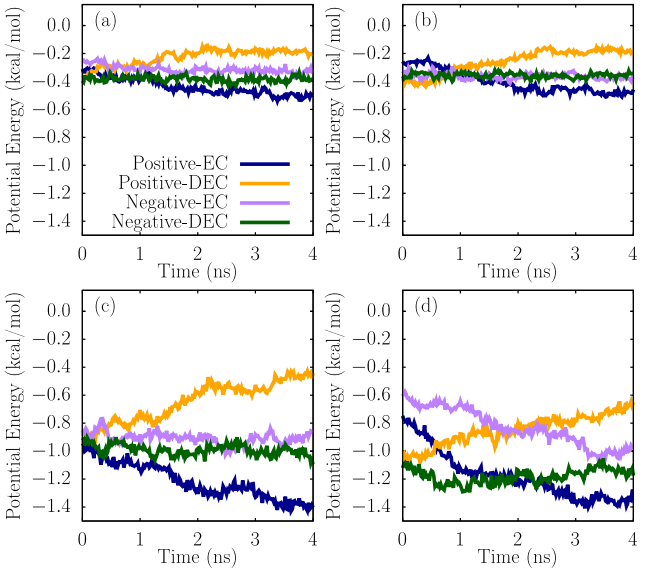

Fig. 11. Interaction energy (Lennard-Jones plus Coulomb) up to 12 Å between solvent molecules (EC and DEC) and electrode under voltage of $\Delta\Psi = 3$ V normalized by the number of electrode atoms. Data for (a) Graphene, (b) Irida-Graphene, (c) Silicene, and (d) Irida-Silicene.

4. Summary and conclusions

This work assessed the capacitive response of 2D electrodes with honeycomb and Irida lattices based on carbon and silicon using fully atomistic molecular dynamics with a constant-potential treatment of electrode polarization. Silicon-based devices exhibited higher specific capacitance, along with reduced cell resistance, compared to their carbon counterparts under the same electrolyte and operating conditions. The improvement is consistent with stronger counterion adsorption and enhanced charge polarization at corrugated silicon surfaces, which together facilitate charging and lessen resistive losses.

The analysis of charging transients, differential capacitance, and effective ion accumulation indicates a coherent picture across structures. Irida-type electrodes exhibit larger charge storage than their honeycomb analogues. Silicon variants further benefit from intrinsic buckling in their distinct morphology that increases the local roughness and accessible interfacial area without requiring pore engineering.

This increased surface roughness enhances charge polarization, strengthens interactions with counterions, and promotes denser ion packing within the electrical double layer. As a result, the electrode can store more charge per unit mass and screen the applied potential more efficiently, leading to higher specific capacitance and lower cell resistance. Although the porous Irida network provides additional adsorption sites, buckling-induced surface roughness emerges as the key morphological feature distinguishing silicon-based materials from their flat carbon analogues. This observation highlights that engineering atomic-scale surface roughness, rather than merely increasing porosity, represents a powerful strategy for improving capacitive performance.

Structural characterization of the electrolyte shows potential-dependent layering near the electrodes and a selective enrichment of EC at charged interfaces. At the same time, cation coordination in the first nanometers remains comparable to the bulk environment. These observations align with reports that interfacial morphology and solvation govern screening and ultimately the capacitive response.

The results suggest two design guidelines. First, atomic-scale corrugation and controlled roughness can be effective levers for improving capacitance without excessive mass penalty. Second, electrolyte formulation should be considered in conjunction with surface morphology, as solvent identity and ion-solvent interactions influence layering, screening length, and resistance. The present conclusions were obtained for $1\,\mathrm{mol\,L^{-1}}$ $NaPF_6$ in EC:DEC at 350 K and planar monolayer electrodes, which sets a clear scope for comparison.

Multiscale models connecting atomistic descriptors of roughness to macroscopic performance are a natural extension. Continued exploration of underexplored 2D allotropes such as Irida-like lattices and related heterostructures is likely to advance supercapacitor research by broadening the materials palette beyond the most established options.

CRediT authorship contribution statement

Hugo X. Rodrigues: Writing – review & editing, Writing – original draft, Visualization, Validation, Software, Methodology, Investigation, Formal analysis. **Isabel A. Silva:** Writing – review & editing, Writing – original draft, Visualization, Validation, Software, Methodology, Investigation, Formal analysis, Data curation, Conceptualization. **Leonardo J.A. Siqueira:** Writing – review & editing, Writing – original draft, Validation, Supervision, Resources, Project administration, Methodology, Investigation, Funding acquisition, Formal analysis, Conceptualization. **Luiz A. Ribeiro Jr.:** Writing – review & editing, Validation, Investigation, Funding acquisition, Formal analysis. **Marcelo L. Pereira Jr.:** Writing – review & editing, Visualization, Validation, Software, Methodology, Investigation, Funding acquisition, Formal analysis.

Declaration of competing interest

The authors declare that they have no known competing financial interests or personal relationships that could have appeared to influence the work reported in this paper.

Acknowledgments

This work received partial support from Brazilian agencies CAPES, CNPq, and FAPDF. MLPJ acknowledges financial support from FAPDF (grant 00193-00001807/2023-16), CNPq (grants 444921/2024-9 and 308222/2025-3), and CAPES (grant 88887.005164/2024-00). LJAS acknowledges CNPq (305756/2023-0), CAPES (88887.964834/2024-00), and FAPESP (2022/11983-4 and 2025/27044-5). IAS thanks the scholarship provided by CAPES (code 001). L.A.R.J. acknowledges the financial support from FAP-DF grants 00193.00001808/2022-71 and 00193-00001857/2023-95, FAPDF-PRONEM grant 00193.00001247/2021-20, PDPG-FAPDF-CAPES Centro-Oeste 00193-00000867/2024-94, and CNPq grants 350176/2022-1 and 167745/2023-9.

Appendix A. Supplementary data

Supplementary material related to this article can be found online at https://doi.org/10.1016/j.est.2026.121121.

Data availability

Data will be made available on request.

References

[1] Z. Xie, B. Zhang, Y. Ge, Y. Zhu, G. Nie, Y. Song, C.-K. Lim, H. Zhang, P.N. Prasad, Chemistry, functionalization, and applications of recent monoelemental two-dimensional materials and their heterostructures, Chem. Rev. 122 (1) (2021) 1127–1207.
[2] K. Khan, A.K. Tareen, M. Aslam, Y. Zhang, R. Wang, Z. Ouyang, Z. Gou, H. Zhang, Recent advances in two-dimensional materials and their nanocomposites in sustainable energy conversion applications, Nanoscale 11 (45) (2019) 21622–21678.
[3] S.S. Varghese, S.H. Varghese, S. Swaminathan, K.K. Singh, V. Mittal, Two-dimensional materials for sensing: graphene and beyond, Electronics 4 (3) (2015) 651–687.
[4] K. Khan, A.K. Tareen, M. Aslam, R. Wang, Y. Zhang, A. Mahmood, Z. Ouyang, H. Zhang, Z. Guo, Recent developments in emerging two-dimensional materials and their applications, J. Mater. Chem. C 8 (2) (2020) 387–440.
[5] A.B. Kaul, Two-dimensional layered materials: Structure, properties, and prospects for device applications, J. Mater. Res. 29 (3) (2014) 348–361.
[6] Q. Zeng, H. Wang, W. Fu, Y. Gong, W. Zhou, P.M. Ajayan, J. Lou, Z. Liu, Band engineering for novel two-dimensional atomic layers, Small 11 (16) (2015) 1868–1884.
[7] K.S. Novoselov, A.K. Geim, S.V. Morozov, D.-e. Jiang, Y. Zhang, S.V. Dubonos, I.V. Grigorieva, A.A. Firsov, Electric field effect in atomically thin carbon films, Science 306 (5696) (2004) 666–669.
[8] S. Jana, A. Bandyopadhyay, S. Datta, D. Bhattacharya, D. Jana, Emerging properties of carbon based 2D material beyond graphene, J. Phys.: Condens. Matter. 34 (5) (2021) 053001.
[9] G. Liu, Z. Zhang, Z. Li, L. Guo, L. Ning, 0D to 2D carbon-based materials in flexible strain sensors: recent advances and perspectives, 2D Mater. 10 (2) (2023) 022002.
[10] Q. Fan, L. Yan, M.W. Tripp, O. Krejčí, S. Dimosthenous, S.R. Kachel, M. Chen, A.S. Foster, U. Koert, P. Liljeroth, et al., Biphenylene network: A nonbenzenoid carbon allotrope, Science 372 (6544) (2021) 852–856.
[11] M.A. Hudspeth, B.W. Whitman, V. Barone, J.E. Peralta, Electronic properties of the biphenylene sheet and its one-dimensional derivatives, ACS Nano 4 (8) (2010) 4565–4570.
[12] A. Balaban, C.C. Rentia, E. Ciupitu, Chemical graphs. 6. Estimation of relative stability of several planar and tridimensional lattices for elementary carbon, Rev. Roum. Chim 13 (2) (1968) 231–247.
[13] L. Hou, X. Cui, B. Guan, S. Wang, R. Li, Y. Liu, D. Zhu, J. Zheng, Synthesis of a monolayer fullerene network, Nature 606 (7914) (2022) 507–510.
[14] S. Berber, E. Osawa, D. Tománek, Rigid crystalline phases of polymerized fullerenes, Phys. Rev. B 70 (8) (2004) 085417.
[15] H. Oughaddou, H. Enriquez, M.R. Tchalala, H. Yildirim, A.J. Mayne, A. Bendounan, G. Dujardin, M. Ait Ali, A. Kara, Silicene, a promising new 2D material, Prog. Surf. Sci. 90 (1) (2015) 46–83.
[16] D. Akinwande, C. Huyghebaert, C.-H. Wang, M.I. Serna, S. Goossens, L.-J. Li, H.-S.P. Wong, F.H. Koppens, Graphene and two-dimensional materials for silicon technology, Nature 573 (7775) (2019) 507–518.
[17] A. Molle, C. Grazianetti, L. Tao, D. Taneja, M.H. Alam, D. Akinwande, Silicene, silicene derivatives, and their device applications, Chem. Soc. Rev. 47 (16) (2018) 6370–6387.

[18] M.P. Júnior, W.F. da Cunha, W.F. Giozza, R.T. de Sousa Junior, L.R. Junior, Irida-graphene: A new 2d carbon allotrope, FlatChem 37 (2023) 100469.
[19] I.M. Felix, R.M. Tromer, L.D. Machado, D.S. Galvão, L.A. Ribeiro, M.L. Pereira, Irida-graphene phonon thermal transport via non-equilibrium molecular dynamics simulations, Nanoscale 16 (2024) 16430–16438.
[20] J. Li, M. Han, S. Zhao, T. Li, T. Yu, Y. Zhang, H.-K. Tang, Q. Peng, Mechanics and crack analysis of irida graphene bilayer composite: A molecular dynamics study, J. Compos. Sci. 7 (12) (2023) 490.
[21] C.P. Bhat, D. Bandyopadhyay, Insights into the reversible hydrogen storage mechanism of transition metal-decorated Irida-graphene: A DFT study, Int. J. Hydrog. Energy 137 (2025) 750–761.
[22] Y. Tan, X. Tao, Y. Ouyang, Q. Peng, Stable and 7.7 wt% hydrogen storage capacity of Ti decorated Irida-Graphene from first-principles calculations, Int. J. Hydrog. Energy 50 (2024) 738–748.
[23] J.A. Laranjeira, W. Elaggoune, N.F. Martins, X. Chen, J.R. Sambrano, OLi3-decorated irida-graphene for high-capacity hydrogen storage: A first-principles study, J. Phys. Chem. Solids (2025) 112951.
[24] L. Yuan, M. Shi, J. Su, D. Wang, H. Zhang, J. Gong, J. Ma, First-principles investigation of Irida-graphene decorated with alkali metal for reversible hydrogen storage, Comput. Theor. Chem. 1239 (2024) 114756.
[25] Y.-F. Zhang, J. Guo, Li-decorated 2d irida-graphene as a potential hydrogen storage material: A dispersion-corrected density functional theory calculations, Int. J. Hydrog. Energy 50 (2024) 1004–1014.
[26] Y. Sun, Y. Chen, M. Yang, K. Zhou, J. Sun, K. Zhao, L. Xu, First-principles study of the hydrogen storage properties of Irida-graphene, Phys. Chem. Chem. Phys. 27 (2) (2025) 915–929.
[27] Z. Duan, S. Shi, C. Yao, X. Liu, K. Diao, D. Lei, Y. Liu, Reversible hydrogen storage with Na-modified Irida-Graphene: A density functional theory study, Int. J. Hydrog. Energy 85 (2024) 1–11.
[28] Y. Zhang, Z. Liu, J. Guo, Z. Cao, J. Wang, Ca-decorated 2D Irida-graphene as a promising hydrogen storage material: A combination of DFT and AIMD study, Int. J. Hydrog. Energy 91 (2024) 118–126.
[29] X. Xiong, H.-B. Cao, Z. Lu, C.-S. Liu, X.-J. Ye, Theoretical prediction on irida-graphene monolayer as promising anode material for lithium-ion batteries, Comput. Mater. Sci. 244 (2024) 113225.
[30] M. Kaur, N. Duhan, T.D. Kumar, Irida-graphene: A new two-dimensional electrode material for sodium-ion batteries, J. Energy Storage 104 (2024) 114456.
[31] N.F. Martins, J.A. Laranjeira, G.S. Fabris, P.A. Denis, J.R. Sambrano, Irida-graphene as a high-performance anode for sodium batteries, J. Energy Storage 104 (2024) 114637.
[32] Y. Wei, X. Zhang, G. Fu, B. Yang, L. Zhang, C63: A promising alkali-ion battery anode material, Diam. Relat. Mater. 148 (2024) 111528.
[33] M.A. Rusho, A.T. Ahmed, A.S. Jasim, P. Kanjariya, A. Rajiv, A. Shankhyan, P.N. Bhakuni, H. Elshafie, A new type of two-dimensional carbon-based monolayers namely irida-graphene as an anode material for magnesium-ion batteries, J. Mol. Graph. Model. 135 (2025) 108934.
[34] M.A. Rusho, A.A. Mutar, P. Kanjariya, A. Rajiv, A. Shankhyan, H.M. Albert, S. Choudhury, Z.A. Abd Alhassan, M.A. Abass, H.M. Alkahtani, Irida-like boron nitride two-dimensional monolayer high-capacity anode for potassium ion battery, Diam. Relat. Mater. 154 (2025) 112223.
[35] N.F. Martins, Y.Z. Abdullahi, J.A. Laranjeira, J.R. Sambrano, Exploring Irida-graphene as an efficient anchoring material for lithium-sulfur batteries: A DFT study, Surf. Interfaces (2025) 107193.
[36] R. Majidi, Irida-graphyne: A promising material for optoelectronic applications, Mater. Today Commun. 38 (2024) 107641.
[37] R. Majidi, A.I. Ayesh, Twin Irida graphene: a carbon material with optoelectronic features, Adv. Theory Simul. 7 (7) (2024) 2400131.
[38] M.L. Pereira Jr., D. da S. Gomes, K.A. Lima, G.D. Nze, F.L. Mendonça, L.A. Ribeiro Jr., Two-dimensional boron nitride allotrope Irida-B12N12 with 3-6-8 membered rings and wide-bandgap semiconducting properties, Sci. Rep. 14 (1) (2024) 28892.
[39] D.d.S. Gomes, L.A. Ribeiro Jr., M.L. Pereira Jr., Predicting Irida-Silicene: A novel 2D silicon allotrope, ACS Omega 9 (51) (2024) 50570–50578.
[40] L.L. Zhang, X.S. Zhao, Carbon-based materials as supercapacitor electrodes, Chem. Soc. Rev. 38 (9) (2009) 2520.
[41] S. Giri, S.K. Nanda, A. Parida, Recent experimental and theoretical progress in silicene based electrode materials for rechargeable batteries and supercapacitors, J. Energy Storage 113 (2025) 115521.
[42] A.M. Sampaio, L.J.A. Siqueira, Ether-functionalized sulfonium ionic liquid and its binary mixtures with acetonitrile as electrolyte for electrochemical double layer capacitors: A molecular dynamics study, J. Phys. Chem. B 124 (2020) 6679–6689.
[43] A.V. Cresce, S.M. Russell, O. Borodin, J.A. Allen, M.A. Schroeder, M. Dai, J. Peng, M.P. Gobet, S.G. Greenbaum, R.E. Rogers, K. Xu, Solvation behavior of carbonate-based electrolytes in sodium ion batteries, Phys. Chem. Chem. Phys. 19 (1) (2017) 574–586.
[44] F. Cheng, M. Cao, Q. Li, C. Fang, J. Han, Y. Huang, Electrolyte salts for sodium-ion batteries: NaPF6 or NaClO4? ACS Nano 17 (18) (2023) 18608–18615.
[45] P. Simon, Y. Gogotsi, Materials for electrochemical capacitors, Nat. Mater. 7 (11) (2008) 845–854.
[46] J.N.C. Lopes, A.A.H. Pádua, Cl&p: A generic and systematic force field for ionic liquids modeling, Theor. Chem. Acc. 131 (2012) 1129.
[47] E. Pluhařová, P.E. Mason, P. Jungwirth, Ion pairing in aqueous lithium salt solutions with monovalent and divalent counter-anions, J. Phys. Chem. A 117 (2013) 11766–11773.
[48] M. Takeuchi, Y. Kameda, Y. Umebayashi, S. Ogawa, T. Sonoda, S. ichi Ishiguro, M. Fujita, M. Sano, Ion–ion interactions of LiPF6 and LiBF4 in propylene carbonate solutions, J. Mol. Liq. 148 (2) (2009) 99–108.
[49] L. Martínez, R. Andrade, E.G. Birgin, J.M. Martínez, PACKMOL: A package for building initial configurations for molecular dynamics simulations, J. Comput. Chem. 30 (2009) 2157–2164.
[50] A. Padua, K. Goloviznina, Z. GONG, agiliopadua/fftool: XML force field files, 2021.
[51] P.H.L. Ferreira, A.M. Sampaio, L.J.A. Siqueira, Energy and power performances of binary mixtures of ionic liquids in planar and porous electrodes by molecular dynamics simulations, Electrochim. Acta 410 (2022) 139982.
[52] R.A. Mendes, L.G. Dias, J.L.D. Silva, L.J. Siqueira, Sodium-ion electrolytes based on poly-ethylene oxide oligomers in dual-carbon cells: Anion size drives the charging behavior, Nano Energy 118 (2023) 108957.
[53] I.A. Silva, E.E. Fileti, L.J.A. Siqueira, Atomistic insights into the superior performance of C60-decorated graphene supercapacitors, J. Mol. Liq. 404 (2024) 124855.
[54] A.M. Sampaio, S. Bi, M. Salanne, L.J. Siqueira, Molecular dynamics simulations of ionic liquids confined into MXenes, Energy Storage Mater. 70 (2024) 103502.
[55] I.A. Silva, A.M. Sampaio, M. Salanne, L.J.A. Siqueira, Unveiling the energy storage of supercapacitors containing water-in-salt electrolytes confined in MXenes by molecular dynamics simulations, J. Mater. Chem. A 13 (2025) 15645–15658.
[56] R. Venâncio, R. Vicentini, M.J.P. C., D.A. Corrêa, A.N. Miranda, A.C. Queiroz, F.T. Degasperi, L.J. Siqueira, L.M.D. Silva, H. Zanin, Combining electrochemical, molecular simulation and operando techniques to investigate the stability of electrodes and organic electrolytes used in EDLCs, Energy Storage Mater. 62 (2023) 102943.
[57] E. Duboué-Dijon, P.E. Mason, H.E. Fischer, P. Jungwirth, Hydration and ion pairing in aqueous Mg 2+ and Zn 2+ solutions: Force-field description aided by neutron scattering experiments and ab initio molecular dynamics simulations, J. Phys. Chem. B 122 (2018) 3296–3306.
[58] T. Méndez-Morales, J. Carrete, M. Pérez-Rodríguez, Ó. Cabeza, L.J. Gallego, R.M. Lynden-Bell, L.M. Varela, Molecular dynamics simulations of the structure of the graphene–ionic liquid/alkali salt mixtures interface, Phys. Chem. Chem. Phys. 16 (2014) 13271–13278.
[59] Y. Zhu, L. Zhang, X. Lu, L. Lu, X. Wu, Flow resistance analysis of nanoconfined water in silt pores by molecular simulations: Effect of pore wall interfacial properties, Fluid Phase Equilib. 362 (2014) 235–241.
[60] R. Hockney, S. Goel, J. Eastwood, A 10000 particle molecular dynamics model with long range forces, Chem. Phys. Lett. 21 (3) (1973) 589–591.
[61] J. Eastwood, Optimal particle-mesh algorithms, J. Comput. Phys. 18 (1) (1975) 1–20.
[62] I.-C. Yeh, M.L. Berkowitz, Ewald summation for systems with slab geometry, J. Chem. Phys. 111 (1999) 3155–3162.
[63] S. Nosé, M. Klein, Constant pressure molecular dynamics for molecular systems, Mol. Phys. 50 (5) (1983) 1055–1076.
[64] W.G. Hoover, Canonical dynamics: Equilibrium phase-space distributions, Phys. Rev. A 31 (1985) 1695–1697.
[65] J.-P. Ryckaert, G. Ciccotti, H.J. Berendsen, Numerical integration of the cartesian equations of motion of a system with constraints: molecular dynamics of n-alkanes, J. Comput. Phys. 23 (3) (1977) 327–341.
[66] S.K. Reed, O.J. Lanning, P.A. Madden, Electrochemical interface between an ionic liquid and a model metallic electrode, J. Chem. Phys. 126 (2007) 084704.
[67] L.J.V. Ahrens-Iwers, M. Janssen, S.R. Tee, R.H. Meißner, ELECTRODE: An electrochemistry package for atomistic simulations, J. Chem. Phys. 157 (2022).
[68] S. Plimpton, Fast parallel algorithms for short-range molecular dynamics, J. Comput. Phys. 117 (1995) 1–19.
[69] D.d.S. Gomes, L.A. Ribeiro, M.L. Pereira, Predicting Irida-Silicene: A novel 2D silicon allotrope, ACS Omega 9 (51) (2024) 50570–50578.
[70] M. Pereira Júnior, W. da Cunha, W. Giozza, R. de Sousa Junior, L. Ribeiro Junior, Irida-graphene: A new 2D carbon allotrope, FlatChem 37 (2023) 100469.
[71] J. Vatamanu, L. Cao, O. Borodin, D. Bedrov, G.D. Smith, On the influence of surface topography on the electric double layer structure and differential capacitance of graphite/ionic liquid interfaces, J. Phys. Chem. Lett. 2 (2011) 2267–2272.
[72] G. Jeanmairet, B. Rotenberg, M. Salanne, Microscopic simulations of electrochemical double-layer capacitors, Chem. Rev. 122 (2022) 10860–10898.
[73] G.F.L. Pereira, E.E. Fileti, L.J.A. Siqueira, Comparing graphite and graphene oxide supercapacitors with a constant potential model, J. Phys. Chem. C 125 (4) (2021) 2318–2326.
[74] C. Péan, C. Merlet, B. Rotenberg, P.A. Madden, P.-L. Taberna, B. Daffos, M. Salanne, P. Simon, On the dynamics of charging in nanoporous carbon-based supercapacitors, ACS Nano 8 (2) (2014) 1576–1583.

[75] C. Pean, B. Rotenberg, P. Simon, M. Salanne, Multi-scale modelling of supercapacitors: From molecular simulations to a transmission line model, J. Power Sources 326 (2016) 680–685.
[76] C. Pean, B. Rotenberg, P. Simon, M. Salanne, Understanding the different (dis)charging steps of supercapacitors: influence of potential and solvation, Electrochim. Acta 206 (2016) 504–512.
[77] R. Venâncio, D.A. da Silva, L.O. Borges, I.A. Silva, L.M. Da Silva, G. Doubek, L.J. Siqueira, H. Zanin, High performance of supercapacitors containing an ionic liquid electrolyte by means of electrochemical and computational studies, Electrochim. Acta 535 (2025) 146569.
[78] C. Merlet, M. Salanne, B. Rotenberg, P.A. Madden, Influence of solvation on the structural and capacitive properties of electrical double layer capacitors, Electrochim. Acta 101 (2013) 262–271.
[79] Z. Hu, J. Vatamanu, O. Borodin, D. Bedrov, A molecular dynamics simulation study of the electric double layer and capacitance of [BMIM][PF6] and [BMIM][BF4] room temperature ionic liquids near charged surfaces, Phys. Chem. Chem. Phys. 15 (2013) 14234.
[80] G.F.L. Pereira, R.G. Pereira, M. Salanne, L.J.A. Siqueira, Molecular dynamics simulations of ether-modified phosphonium ionic liquid confined in between planar and porous graphene electrode models, J. Phys. Chem. C 123 (2019) 10816–10825.
[81] A.J.P. Neto, E.E. Fileti, Differential capacitance and energetics of the electrical double layer of graphene oxide supercapacitors: Impact of the oxidation degree, J. Phys. Chem. C 122 (2018) 21824–21832.
[82] G. Feng, J. Huang, B.G. Sumpter, V. Meunier, R. Qiao, A "counter-charge layer in generalized solvents" framework for electrical double layers in neat and hybrid ionic liquid electrolytes, Phys. Chem. Chem. Phys. 13 (2011) 14723.
[83] C. Merlet, B. Rotenberg, P.A. Madden, P.-L. Taberna, P. Simon, Y. Gogotsi, M. Salanne, On the molecular origin of supercapacitance in nanoporous carbon electrodes, Nat. Mater. 11 (2012) 306–310.
[84] Z. Lin, D. Barbara, P.-L. Taberna, K.L. Van Aken, B. Anasori, Y. Gogotsi, P. Simon, Capacitance of Ti3C2Tx MXene in ionic liquid electrolyte, J. Power Sources 326 (2016) 575–579.
[85] R. Jorn, R. Kumar, D.P. Abraham, G.A. Voth, Atomistic modeling of the electrode–electrolyte interface in li-ion energy storage systems: Electrolyte structuring, J. Phys. Chem. C 117 (8) (2013) 3747–3761.
[86] G.-y. Cui, Z.-l. Yi, F.-y. Su, C.-m. Chen, P.-d. Han, A DFT study of the effect of stacking on the quantum capacitance of bilayer graphene materials, New Carbon Mater. 36 (6) (2021) 1062–1070.
[87] G.M. Yang, H.Z. Zhang, X.F. Fan, W.T. Zheng, Density functional theory calculations for the quantum capacitance performance of graphene-based electrode material, J. Phys. Chem. C 119 (12) (2015) 6464–6470.
[88] Y. Zou, A.S. Walton, I.A. Kinloch, R.A.W. Dryfe, Investigation of the differential capacitance of highly ordered pyrolytic graphite as a model material of graphene, Langmuir 32 (44) (2016) 11448–11455.
[89] Z. Wen, X. Wang, S. Mao, Z. Bo, H. Kim, S. Cui, G. Lu, X. Feng, J. Chen, Crumpled nitrogen-doped graphene nanosheets with ultrahigh pore volume for high-performance supercapacitor, Adv. Mater. 24 (41) (2012) 5610–5616.
[90] Q. Peng, X. Wen, S. De, Mechanical stabilities of silicene, RSC Adv. 3 (33) (2013) 13772.
[91] S. Ghosh, S.K. Behera, A. Mishra, C.S. Casari, K.K. Ostrikov, Quantum capacitance of two-dimensional-material-based supercapacitor electrodes, Energy Fuels 37 (23) (2023) 17836–17862.
[92] T. Mo, S. Bi, Y. Zhang, V. Presser, X. Wang, Y. Gogotsi, G. Feng, Ion structure transition enhances charging dynamics in subnanometer pores, ACS Nano 14 (2020) 2395–2403.
[93] Y. Wang, Y. Song, Y. Xia, Electrochemical capacitors: mechanism, materials, systems, characterization and applications, Chem. Soc. Rev. 45 (21) (2016) 5925–5950.